

## Article

# Synthesis, Structures and Photophysical Properties of Tetra- and Hexanuclear Zinc Complexes Supported by Tridentate Schiff Base Ligands

Tobias Severin <sup>1</sup>, Viktoriia Karabtsova <sup>1</sup>, Martin Börner <sup>1</sup>, Hendrik Weiske <sup>2</sup>, Agnieszka Kuc <sup>3</sup> and Berthold Kersting <sup>1,\*</sup>

<sup>1</sup> Institut für Anorganische Chemie, Universität Leipzig, Johannisallee 29, 04103 Leipzig, Germany; tobias.severin@uni-leipzig.de (T.S.); karabtsovavictoria@gmail.com (V.K.); martin.boerner@uni-leipzig.de (M.B.)

<sup>2</sup> Willhelm-Ostwald-Institut für Physikalische und Theoretische Chemie, Universität Leipzig, Linnéstraße 2, 04103 Leipzig, Germany; hendrik.weiske@uni-leipzig.de

<sup>3</sup> Helmholtz-Zentrum Dresden-Rossendorf, Abteilung Ressourcenökologie, Forschungsstelle Leipzig, Permoserstr. 15, 04318 Leipzig, Germany; a.kuc@hzdr.de

\* Correspondence: b.kersting@uni-leipzig.de; Fax: +49-(0)-341-97-36199

**Abstract:** The synthesis, structure and photophysical properties of two polynuclear zinc complexes, namely  $[\text{Zn}_6\text{L}_2(\mu_3\text{-OH})_2(\text{OAc})_8]$  (**1**) and  $[\text{Zn}_4\text{L}_4(\mu_2\text{-OH})_2](\text{ClO}_4)_2$  (**2**), supported by tridentate Schiff base ligand 2,6-bis((*N*-benzyl)iminomethyl)-4-*tert*-butylphenol (**HL**) are presented. The synthesized compounds were investigated using ESI-MS, IR, NMR, UV-vis absorption spectroscopy, photoluminescence spectroscopy and single-crystal X-ray crystallography. The hexanuclear neutral complex **1** comprises six-, five- and four-coordinated  $\text{Zn}^{2+}$  ions coordinated by O and N atoms from the supporting ligand and OH- and acetate ligands. The  $\text{Zn}^{2+}$  ions in complex cation  $[\text{Zn}_4\text{L}_4(\mu_2\text{-OH})_2]^{2+}$  of **2** are all five-coordinated. The complexation of ligand **HL** by  $\text{Zn}^{2+}$  ions leads to a six-fold increase in the intensity and a large blue shift of the ligand-based  $^1(\pi\text{-}\pi)^*$  emission. Other biologically relevant ions, i.e.,  $\text{Na}^+$ ,  $\text{K}^+$ ,  $\text{Mg}^{2+}$ ,  $\text{Ca}^{2+}$ ,  $\text{Mn}^{2+}$ ,  $\text{Fe}^{2+}$ ,  $\text{Co}^{2+}$ ,  $\text{Ni}^{2+}$  and  $\text{Cu}^{2+}$ , did not give rise to a fluorescence enhancement.

**Keywords:** salicylaldiminato ligands; zinc; coordination geometry; photophysical properties

**Citation:** Severin, T.; Karabtsova, V.; Börner, M.; Weiske, H.; Kuc, A.; Kersting, B. Synthesis, Structures and Photophysical Properties of Tetra- and Hexanuclear Zinc Complexes Supported by Tridentate Schiff Base Ligands. *Chemistry* **2023**, *5*, 1028–1045. <https://doi.org/10.3390/chemistry5020070>

Academic Editor: Roland C. Fischer

Received: 3 April 2023

Revised: 24 April 2023

Accepted: 28 April 2023

Published: 2 May 2023



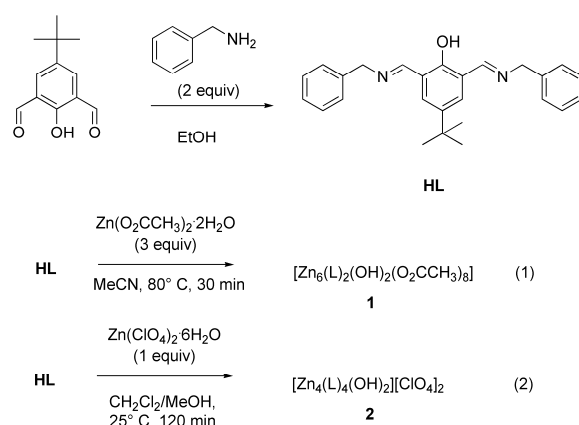
**Copyright:** © 2023 by the authors. Licensee MDPI, Basel, Switzerland. This article is an open access article distributed under the terms and conditions of the Creative Commons Attribution (CC BY) license (<https://creativecommons.org/licenses/by/4.0/>).

## 1. Introduction

Zinc as an essential trace metal for all living organisms is omnipresent in biogenic systems, such as in the cells of the human body. Meanwhile, it is well-known that  $\text{Zn}^{2+}$  greatly contributes to biological processes, for example, as part of the immune system, as an active site or co-factor in enzymes or as a regulator for proteins, and it can also provide a stabilizing function to their structure [1–10]. The  $\text{Zn}^{2+}$  ions can, however, also have toxic effects when toothier concentrations are too high, and it is presumably involved in the biochemical mechanisms of neuronal diseases [4,11]. Proper detection of free zinc, also in living cells, is highly desirable, but it still remains a challenge for common spectroscopic methods, with which free zinc is not obtainable. As a  $d^{10}$  metal,  $\text{Zn}^{2+}$  cannot be observed using UV-vis spectroscopy, but it is particularly suitable for fluorescence spectroscopy. For this technique, the CHEF effect (*chelation-enhanced fluorescence effect*) is exploited for a strong augmentation in the fluorescence intensity of the sensor molecule. Usually, the PET (*photoinduced electron transfer*) quenches the luminescence of some chemosensors, and it is turned off by the complexation of the closed-shell  $d^{10}$  metal ion [12–23]. This combines two important factors: the high sensitivity of fluorescence spectroscopy and the excellent selectivity for  $\text{Zn}^{2+}$ . A set of molecules, which provide these abilities, were already

designed and explored: for example, 8-aminoquinoline-based sensor molecules such as 6-methoxy-(8-*p*-toluenesulfonamide)quinoline (TSQ), Zinquin (ZQ) and 2-(hydroxymethyl)-4-methyl-6-((quinolinyl-8-imino)methyl)phenol (HMQP) [24–30]. However, what is often left out from consideration is the influence of different anions that may disturb the mechanism of complexation with zinc and the sensitivity of the method.

Recently, we have reported the synthesis, structures and properties of some discrete four- and five-coordinated  $\text{Zn}^{2+}$  complexes supported by salicylaldiminato ligands [31–35]. As an extension, here, we report the synthesis of two zinc complexes derived from new Schiff base ligand **HL** (Scheme 1) bearing two imine functions and a phenolic oxygen as a N,O,N-donor set. The effect of the metal–ligand ratio variations on the coordination and luminescence properties is reported. The results are supported by accompanying DFT calculations of UV/vis spectra.



**Scheme 1.** Synthesis of ligand **HL** and zinc complexes **1** and **2**.

## 2. Materials and Methods

All reagents were purchased and used without any further purification. 4-*tert*-butyl-2,6-diformylphenol was purchased from Sigma Aldrich. Solvents were of HPLC grade and not additionally purified. UV/vis spectra were recorded with a V-670 spectrophotometer from JASCO and analyzed with SPECTRA MANAGER v2.05.03 software. HELLMA 110-QS quartz cells with 10 mm path length were used as cuvettes. Measurements were made within the range of 190–650 nm. Fluorescence spectra were recorded on a Perkin Elmer FL6500 spectrometer using a constant slit width. Data acquisition was performed using the FL WINLAB v3.00 program from PERKINELMER [36]. Measurements were performed using precision SUPRASIL type 111-10-40-QS fused silica cells (10 mm cell diameter, 3500  $\mu\text{L}$  volume) from HELLMA ANALYTICS. The infrared spectra were recorded with a Bruker Vertex 80V FTIR spectrometer utilizing KBr pellets. The ORIGINPRO 8G program from ORIGINLAB CORPORATION was used for data analysis and a graphical display of the spectra [37].  $^1\text{H}$  and  $^{13}\text{C}$  NMR spectra measurements were recorded on BRUKER model DPX-400 ( $^1\text{H}$ : 400 MHz;  $^{13}\text{C}$ : 100 MHz) or VARIAN Gemini 300 instruments ( $^1\text{H}$ : 300 MHz;  $^{13}\text{C}$ : 75 MHz). The solvent signal served as the internal standard. The MestReNova v11.0 program from MESTRELAB RESEARCH S. L. was utilized for data analyses and graphical displays [38]. ESI mass spectra were recorded using MICROTOF or IMPACT II mass spectrometers from BRUKER DALTONIK GMBH. Elemental analyses were measured using an ELEMENTAR VARIO EL instrument from ELEMENTAR ANALYSESYSTEME GMBH.

**X-ray crystallography.** Single-crystal X-ray diffraction experiments were carried out on a STOE STADIVARI, equipped with an X-ray micro-source ( $\text{Cu-K}\alpha$ ,  $\lambda = 1.54186 \text{ \AA}$ ) and a DECTRIS Pilatus 300K detector at 180(2) K. The diffraction frames were processed with the STOE X-RED software package [39]. The structures were solved by direct methods [40] and refined by full-matrix least-squares techniques on the basis of all data against  $F^2$  using

SHELXL-2018/3 [41]. PLATON was used to search for higher symmetry [42]. All non-hydrogen atoms were refined anisotropically. H atoms were placed in calculated positions and allowed to ride on their respective C atoms and treated isotropically using the 1.2- or 1.5-fold  $U_{\text{iso}}$  value of the parent C atoms. All non-hydrogen atoms were refined anisotropically. All calculations were performed using the Olex2 crystallographic platform [43]. ORTEP-3 and POV-RAY were used for the artwork of the structures [44]. CCDC 2248758–2248760 contains the supplementary crystallographic data for this paper.

**Crystallographic data for 2,6-(BzN=CH)-4-*t*Bu-C<sub>6</sub>H<sub>2</sub>OH.** C<sub>26</sub>H<sub>28</sub>N<sub>2</sub>O,  $M_r = 384.50$  g/mol, triclinic, space group  $P-1$ ,  $a = 8.3627(2)$  Å,  $b = 10.9002(3)$  Å,  $c = 11.8113(4)$  Å,  $\alpha = 100.761(2)^\circ$ ,  $\beta = 94.116(2)^\circ$ ,  $\gamma = 91.320(2)^\circ$ ,  $V = 1054.27(5)$  Å<sup>3</sup>,  $Z = 2$ ,  $\rho_{\text{calcd}} = 1.211$  g/cm<sup>3</sup>,  $T = 180(2)$  K,  $\mu(\text{Cu-K}\alpha)$ ,  $\lambda = 1.54186$  Å, crystal size  $0.326 \times 0.307 \times 0.256$  mm<sup>3</sup>, 19,262 reflections measured, 3908 unique, 3518 with  $I > 2\sigma(I)$ . Final  $R_1 = 0.0372$  ( $I > 2\sigma(I)$ ),  $wR_2 = 0.1057$  (3908 refl.), 267 parameters and 0 restraints, min./max. residual electron density =  $-0.181/0.254$  e<sup>−</sup>/Å<sup>3</sup>.

**Crystallographic data for 1·3MeCN·0.5H<sub>2</sub>O.** C<sub>74</sub>H<sub>90</sub>N<sub>7</sub>O<sub>20.5</sub>Zn<sub>6</sub>,  $M_r = 1806.88$  g/mol, triclinic, space group  $P-1$ ,  $a = 9.9260(3)$  Å,  $b = 15.0044(5)$  Å,  $c = 28.7383(7)$  Å,  $\alpha = 98.943(2)^\circ$ ,  $\beta = 92.514(2)^\circ$ ,  $\gamma = 104.406(2)^\circ$ ,  $V = 4079.9(2)$  Å<sup>3</sup>,  $Z = 2$ ,  $\rho_{\text{calcd}} = 1.471$  g/cm<sup>3</sup>,  $T = 180(2)$  K,  $\mu(\text{Cu-K}\alpha)$ ,  $\lambda = 1.54186$  Å, crystal size  $0.160 \times 0.090 \times 0.050$  mm<sup>3</sup>, 70,648 reflections measured, 14,641 unique, 7769 with  $I > 2\sigma(I)$ . Final  $R_1 = 0.0577$  ( $I > 2\sigma(I)$ ),  $wR_2 = 0.1521$  (14641 refl.), 1140 parameters and 402 restraints, min./max. residual electron density =  $-0.609/1.000$  e<sup>−</sup>/Å<sup>3</sup>. The *tert*-butyl groups are disordered over two positions (0.66/0.34 and 0.53/0.47) and restrained with SADI, RIGU, DELU, and SIMU. One benzyl group of each ligand is disordered over two positions (0.51/0.49 and 0.72/0.28), restrained with SADI, SIMU, DELU, and RIGU. AFIX 66 was used to fix both benzene rings. One methylene group was constrained with EADP. One MeCN is disordered over two positions (0.74/0.26), restrained with DFIX (1.137 and 2.593), SIMU, and RIGU. The nitrogen atom was constrained with EADP. The solvent water molecule is disordered over a special position and was modeled with PART -1. Crystals of 1·3MeCN·0.5H<sub>2</sub>O grown by recrystallization of 1·4H<sub>2</sub>O from MeCN solution quickly lost solvate molecules upon standing in air and became turbid.

**Crystallographic data for 2·3MeOH·0.5MeCN.** C<sub>108</sub>H<sub>123.5</sub>Cl<sub>2</sub>N<sub>8.5</sub>O<sub>17</sub>Zn<sub>4</sub>,  $M_r = 2145.03$  g/mol, monoclinic, space group  $P2_1/n$ ,  $a = 17.9667(4)$  Å,  $b = 30.1926(5)$  Å,  $c = 19.4877(4)$  Å,  $\alpha = 90^\circ$ ,  $\beta = 92.875(2)^\circ$ ,  $\gamma = 90^\circ$ ,  $V = 10,558.0(4)$  Å<sup>3</sup>,  $Z = 4$ ,  $\rho_{\text{calcd}} = 1.349$  g/cm<sup>3</sup>,  $T = 180(2)$  K,  $\mu(\text{Cu-K}\alpha)$ ,  $\lambda = 1.54186$  Å, crystal size  $0.186 \times 0.154 \times 0.121$  mm<sup>3</sup>, 101,721 reflections measured, 19,944 unique, 10,877 with  $I > 2\sigma(I)$ . Final  $R_1 = 0.0477$  ( $I > 2\sigma(I)$ ),  $wR_2 = 0.1328$  (19,944 refl.), 1403 parameters and 492 restraints, min./max. residual electron density =  $-0.572/0.767$  e<sup>−</sup>/Å<sup>3</sup>. One *tert*-butyl group is disordered over two positions (0.72/0.28), restrained with DFIX (1.54), SADI, SIMU, and RIGU. One benzyl group is disordered over two positions (0.72/0.28), restrained with SIMU and RIGU. AFIX 66 was used to fix the benzene rings, and the methylene group was constrained with EADP. The perchlorate ion is disordered over two positions (0.59/0.41) and restrained with SADI, SIMU, and RIGU. Crystals of 2·3MeOH·0.5MeCN grown by the recrystallization of 2·H<sub>2</sub>O from the MeCN/MeOH solution quickly lost solvate molecules upon standing in air and became turbid.

**Synthesis of 2,6-bis-((N-benzyl)iminomethyl)-4-*tert*-butylphenol (HL).** Benzylamine (546 mg, 5.09 mmol, 2.10 eq.) was added to a solution of 5-*tert*-butyl-2-hydroxybenzene-1,3-dialdehyde (500 mg, 2.42 mmol, 1.00 eq.) in EtOH (20 mL). The resulting yellow solution was stirred for 2 h at ambient temperature to produce a yellow solid, which was isolated by filtration, washed with little cold EtOH and dried at 60°C. The compound was recrystallized once from EtOH to produce a pure product: yellow X-ray quality crystals. Yield: 915 mg (98.2 %). M.p. 122 °C. <sup>1</sup>H-NMR (400 MHz, CD<sub>2</sub>Cl<sub>2</sub>):  $\delta = 1.32$  (s, 9H, CH<sub>3</sub>-*t*Bu), 4.81 (s, 4H, CH<sub>2</sub>), 7.24–7.39 (m, 12H, CH<sup>ar</sup>), 8.70 (s, 2H, N=CH), 13.91 (s, 1H, OH<sup>ar</sup>). <sup>13</sup>C{<sup>1</sup>H}-NMR (100 MHz, DMSO, 90 °C):  $\delta = 30.7$  (CH<sub>3</sub>), 33.3 (C(CH<sub>3</sub>)<sub>3</sub>), 62.4 (CH<sub>2</sub>), 120.5 (*o*-C<sup>ar</sup>), 126.5 (*p*-Bz-C<sup>ar</sup>), 127.4 (*o*-Bz-C<sup>ar</sup>), 127.9 (*m*-Bz-C<sup>ar</sup>), 128.4 (*m*-C<sup>ar</sup>), 138.7

(*ipso*-Bz-*C<sup>ar</sup>*), 140.0 (*p*-*C<sup>ar</sup>*-*t*Bu), 158.8 (*ipso*-*C<sup>ar</sup>*-OH), 161.4 (HC=N). FT-IR (KBr):  $\tilde{\nu}/\text{cm}^{-1}$  = 3083/3059/3028 (w,  $\nu\text{C-H}^{\text{ar}}$ ), 2954/2904/2837 (s-w,  $\nu\text{C-H}$ ), 1633 (s,  $\nu\text{C=N}$ ), 1598 (w,  $\nu\text{C=C}$ ), 1472 (s,  $\delta_{\text{asym.}}$  -CH<sub>3</sub>, *t*Bu), 1439 (s,  $\nu\text{C}^{\text{ar}}$ -O), 1388/1372 (w,  $\delta_{\text{sym.}}$  -CH<sub>3</sub>, *t*Bu), 1287 (m), 1260 (m), 1225 (m), 1203 (w), 1118 (w), 1062 (m), 1027 (w), 942 (w), 882 (w), 844 (w), 823 (w), 750 (s), 718 (w), 699 (s).  $m/z$  (ESI<sup>+</sup>, MeCN): C<sub>26</sub>H<sub>29</sub>N<sub>2</sub>O (384.23) [M + H]<sup>+</sup> calcd: 385.24; found 385.23. UV-vis (DCM/MeOH (3:2/v:v); 5.0·10<sup>-5</sup> M):  $\lambda_{\text{max}}/\text{nm}$  ( $\epsilon/\text{M}^{-1}\text{cm}^{-1}$ ) = 248 (28,090), 348 (5480), 451 (5610); (MeCN; 2.5·10<sup>-5</sup> M):  $\lambda_{\text{max}}/\text{nm}$  ( $\epsilon/\text{M}^{-1}\text{cm}^{-1}$ ) = 193 (56,650), 244 (43,210), 347 (7950), [444 (500)]. Elemental analysis for C<sub>26</sub>H<sub>28</sub>N<sub>2</sub>O (384.51) calc. C 81.21, H 7.34, N 7.29%; found. C 80.92, H 7.36, N 7.23%.

**Synthesis [Zn<sub>6</sub>(L)<sub>2</sub>(OH)<sub>2</sub>(OAc)<sub>8</sub>] (1).** A solution of Zn(OAc)<sub>2</sub>·2H<sub>2</sub>O (190 mg, 866 mmol, 3.00 eq.) in 3 mL of MeCN was added to a solution of **HL** (111 mg, 289 mmol, 1.00 eq.) in MeCN (20 mL). The yellow solution intensified its color and was stirred for 30 min at 80 °C. The solution was left to stand for 2 weeks. The resulting solid was isolated by filtration and dried in air. Yield: 420 mg (86.9%). Elemental analysis for [Zn<sub>6</sub>L<sub>2</sub>(OH)<sub>2</sub>(OAc)<sub>8</sub>]·4H<sub>2</sub>O (C<sub>68</sub>H<sub>88</sub>N<sub>4</sub>O<sub>24</sub>Zn<sub>6</sub>) (1737.8) calc. C 47.00, H 5.10, N 3.22%; found. C 46.97, H 4.62, N 3.10 %. This so isolated powder (1.4H<sub>2</sub>O) was used for all spectroscopic measurements. <sup>1</sup>H-NMR (300 MHz, CD<sub>2</sub>Cl<sub>2</sub>):  $\delta$  = 1.25/1.29 (s, 18H, CH<sub>3</sub>-*t*Bu), 1.73 (s, 24H, CH<sub>3</sub>-OAc), 4.84/5.08 (s, 8H, CH<sub>2</sub>), 7.11–7.42 (m, 20 H, Bz-CH<sup>ar</sup>) 7.47–7.54, (m, 4H, *m*-CH<sup>ar</sup>), 8.31/8.36 (s, 4H, N=CH) ppm. FT-IR (KBr pellet):  $\tilde{\nu}/\text{cm}^{-1}$  = 3029 (w,  $\nu\text{C-H}$ , ar), 2961 (w,  $\nu\text{C-H}$ ), 1604/1580 (s, antisymm.  $\nu\text{C-O}$ , COO<sup>-</sup>), 1415 (s, symm.  $\nu\text{C-O}$ , COO<sup>-</sup>), 1344 (w), 1233 (w,  $\nu\text{C}^{\text{ar}}$ -O), 1066 (w), 1026 (w), 843 (w), 823 (w), 776 (w), 758 (w), 698 (w), 670 (w).  $m/z$  (ESI<sup>+</sup>, MeCN): For [Zn<sub>2</sub>L<sub>2</sub>OAc]<sup>+</sup> as C<sub>54</sub>H<sub>57</sub>N<sub>4</sub>O<sub>4</sub>Zn<sub>2</sub><sup>+</sup> (956.83) [M]<sup>+</sup> calcd: 957.29; found 957.28. UV-vis (DCM/MeOH (3:2 ratio); 2.5 × 10<sup>-5</sup> M):  $\lambda_{\text{max}}/\text{nm}$  ( $\epsilon/\text{M}^{-1}\text{cm}^{-1}$ ) = [221 (16,160)], 260 (30,700), 387 (10,060).

**Synthesis of [Zn<sub>4</sub>L<sub>4</sub>(OH)<sub>2</sub>](ClO<sub>4</sub>)<sub>2</sub> (2).** A solution of Zn(ClO<sub>4</sub>)<sub>2</sub>·6H<sub>2</sub>O (107 mg, 286 mmol, 1.10 eq.) in a few drops of acetonitrile was added to a solution of **HL** (100 mg, 260 mmol, 1.00 eq.) in 20 mL of DCM/MeOH (3:2). The yellow solution intensified its colour and was stirred for 2 h at 40 °C. The solution was left to stand for 2 weeks. The resulting solid was isolated by filtration and dried in air. Yield: 456 mg (86.4%). Elemental analysis for [Zn<sub>4</sub>L<sub>4</sub>(OH)<sub>2</sub>](ClO<sub>4</sub>)<sub>2</sub>·H<sub>2</sub>O (2046.50) calc. C 61.04, H 5.52, N 5.48%; found. C 61.15, H 5.81, N 5.61%. This isolated powder (2·H<sub>2</sub>O) was used for all spectroscopic measurements. <sup>1</sup>H-NMR (300 MHz, CD<sub>2</sub>Cl<sub>2</sub>):  $\delta$  = 1.39 (s, 36H, CH<sub>3</sub>-*t*Bu), 3.55/3.81/4.36 (m, 16H, CH<sub>2</sub>), 6.38–7.46 (m, 48 H, CH<sup>ar</sup>), 7.83/8.13 (s, 8H, N=CH) ppm. FTIR (KBr):  $\tilde{\nu}/\text{cm}^{-1}$  = 3063/3031 (w,  $\nu\text{C-H}$ , ar), 2958/2921 (m,  $\nu\text{C-H}$ ), 1653/1631 (s,  $\nu\text{C=N}$ ), 1542 (s,  $\nu\text{C=C}$ ), 1454 (m,  $\delta_{\text{antisymm}}$  -CH<sub>3</sub>), 1398 (w), 1363 (w), 1233 (m,  $\nu\text{C}^{\text{ar}}$ -O), 1090 (s,  $\nu\text{Cl-O}$ , perchlorate), 928 (w), 878 (w), 840 (w), 759 (m), 700 (m), 625 (s,  $\delta\text{Cl-O}$ , perchlorate).  $m/z$  (ESI<sup>+</sup>, DCM): For [Zn<sub>2</sub>L<sub>2</sub>ClO<sub>4</sub>]<sup>+</sup> as C<sub>52</sub>H<sub>54</sub>ClN<sub>4</sub>O<sub>6</sub>Zn<sub>2</sub><sup>+</sup> (997.24) [M]<sup>+</sup> calcd: 997.23; found 997.22. UV-vis (DCM/MeOH (3:2 ratio); 2.5·10<sup>-5</sup> M):  $\lambda_{\text{max}}/\text{nm}$  ( $\epsilon/\text{M}^{-1}\text{cm}^{-1}$ ) = [228 (18,650)], 257 (27,900), 387 (8800).

**Time-dependent density functional theory.** All structures were optimized using PBE/TZ2P-D3(BJ) [45–47], and the 20 lowest singlet excitations were calculated using TD-DFT [48] at the CAMY-B3LYP [49–51] level of the theory, as implemented in AMS [52–54]. Implicit solvation model COSMO [55–57] was included in all calculations.

### 3. Results

#### 3.1. Synthesis and Characterization of Compounds

The new di-imine ligand **HL** was prepared according to the route provided in Scheme 1. A mixture of 5-*tert*-butyl-2-hydroxybenzene-1,3-dialdehyde and two equivalents of benzylamine were allowed to react in a 1:2 molar ratio at room temperature for 2 h in EtOH in order to provide an intense yellow solution, from which the pure product could be isolated as a yellow microcrystalline solid in an almost quantitative yield.

Two new zinc(II) complexes, **1** and **2**, were prepared according to the reactions in Scheme 1. The reaction of the ligand **HL** with  $\text{Zn}(\text{OAc})_2 \cdot 2\text{H}_2\text{O}$  in a 3:1 ratio in acetonitrile at 80 °C for 30 min produced a pale yellow solution, from which a pale yellow, microcrystalline powder of composition  $[(\text{Zn}_6(\text{L})_2(\text{OH})_2(\text{OAc})_8)] \cdot 4\text{H}_2\text{O}$  (**1**) was reproducibly obtained in ca 87 % yield. The treatment of **HL** with  $\text{Zn}(\text{ClO}_4)_2 \cdot 6\text{H}_2\text{O}$  in a 1:1 ratio in a  $\text{CH}_2\text{Cl}_2/\text{MeOH}/\text{MeCN}$  mixed solvent system furnished a yellow solution, from which a pale yellow solid of composition  $[\text{Zn}_4\text{L}_4(\text{OH})_2](\text{ClO}_4)_2 \cdot \text{H}_2\text{O}$  (**2**) precipitated in an 86 % yield. Both complexes exhibit good solubility in acetonitrile, DMSO and dichloromethane, but they are only sparingly soluble in alcohols and various hydrocarbons and virtually insoluble in water. The synthesized compounds resulted in a satisfactory elemental analyses, and their formulation was confirmed by electrospray ionization mass spectrometry (ESI-MS), FT-IR-spectroscopy, UV-vis and NMR spectroscopy as well as single-crystal X-ray diffractometric analyses.

The infrared spectrum of the free ligand shows a prominent band at  $1634\text{ cm}^{-1}$ , which can be attributed to the  $\text{C}=\text{N}$  stretching frequencies of the imine groups (Figure S1). The O-H stretching appears as a very broad band with a maximum at around  $2600\text{ cm}^{-1}$ , indicating the presence of intramolecular hydrogen bonding interactions between the OH and imine groups. The IR spectrum of zinc complex **1** reveals two bands at  $1580$  and  $1415\text{ cm}^{-1}$  attributed to the antisymmetric and symmetric stretching vibrations of the acetato ligand (Figure S2). The imine group gives rise to two weak features at  $1650$  and  $1630\text{ cm}^{-1}$ . The IR spectrum of perchlorate salt **2** (Figure S2) reveals two strong absorption bands at  $1090$  and  $625\text{ cm}^{-1}$ , characteristic values for the vibrations of a  $\text{ClO}_4^-$  counter anion. Again, as in **1**, there are two bands at  $1653$  and  $1631\text{ cm}^{-1}$  attributable to the stretching vibrations of a coordinated imine group.

### 3.2. Crystallographic Characterization

Single crystals of **HL** obtained from EtOH are triclinic and fall into space group  $P\bar{1}$ . The structure shown in Figure 1 reveals that both imino groups are (*E*)-configured and coplanar with the phenol ring. The phenolic OH group forms an intramolecular hydrogen bond ( $\text{O1-H1-N1}$ ) with the imine group as observed in other salicylaldimines. Figure S5 displays the packing diagram of **HL**. As observed, the phenol rings of two adjacent molecules are engaged in *face-to-face*  $\pi$ - $\pi$  stacking interactions, as manifested by an interplanar distance of  $3.4286(11)\text{ \AA}$ . The DFT-optimized geometry of the **HL** ligand at the PBE/TZ2P-D3(BJ) level of theory is in agreement with the experimental data (Figure S16).

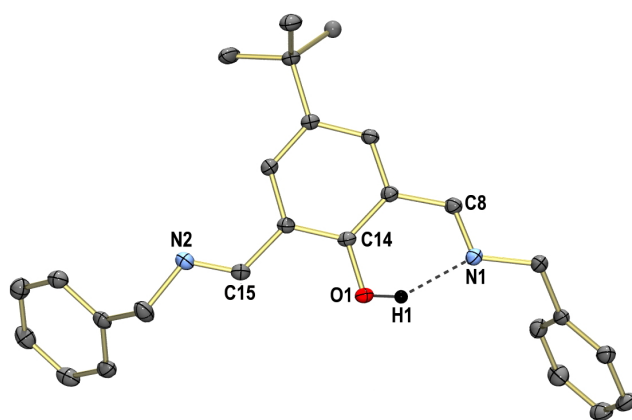


**Figure 1.** Molecular structure of the ligand **HL** in the crystal. Thermal ellipsoids are drawn at the 50% probability level. Hydrogen atoms are omitted for clarity, except one involved in intramolecular hydrogen bonding. Selected bond lengths (Å):  $\text{N1-C8}$   $1.2765(11)$ ,  $\text{N2-C15}$   $1.2677(16)$  and  $\text{O1}\cdots\text{N1}$   $2.5905(12)$ .

Crystals of  $[\text{Zn}_6\text{L}_2(\text{OH})_2(\text{OAc})_8] \cdot 3\text{MeCN} \cdot 0.5\text{H}_2\text{O}$  were grown by the slow evaporation of an acetonitrile solution. The crystal structure comprises a discrete, hexanuclear, mixed-ligand complex,  $[\text{Zn}_6\text{L}_2(\text{OH})_2(\text{OAc})_8]$  (**1**), and several co-crystallized MeCN and  $\text{H}_2\text{O}$  molecules. Figure 2 shows the structure of the neutral zinc complex. The zinc complex exhibits idealized  $\text{C}_2$  symmetry (neglecting the four benzyl groups of the supporting ligand). Two nearly isostructural  $[\text{Zn}_3\text{L}(\text{OH})(\text{OAc})_2]^{2+}$  moieties are connected by four  $\mu_{1,3}$ -bridging acetate groups.

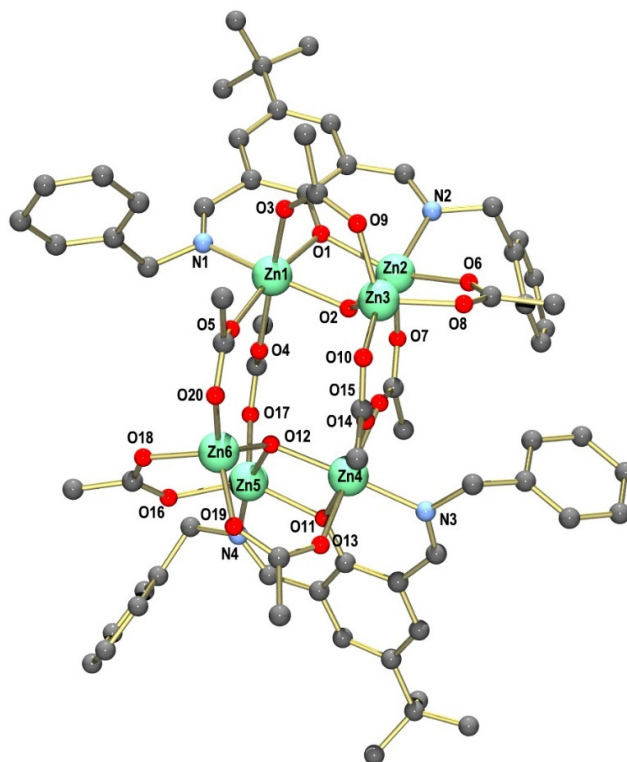


**Figure 2.** Ball and stick representation of the molecular structure of neutral complex **1** in crystals of  $[\text{Zn}_6\text{L}_2(\text{OH})_2(\text{OAc})_8] \cdot 3\text{MeCN} \cdot 0.5\text{H}_2\text{O}$  ( $1 \cdot 3\text{MeCN} \cdot 0.5\text{H}_2\text{O}$ ). Hydrogen atoms are omitted for clarity.

The three  $\text{Zn}^{2+}$  ions within the trinuclear subunits exhibit different coordination environments: Zn1 is six-coordinated by the imine N and phenolate O donors from the supporting ligand, three O atoms from three  $\mu_{1,3}$ -bridging acetato ligands and one triply bridging OH group in a distorted octahedral fashion. The Zn2 atom, on the other hand, is five-coordinated, being surrounded by imine N and phenolate O donors, two O atoms from two  $\mu_{1,3}$ -bridging acetates and the OH bridge. The coordination geometry of Zn2 is severely distorted and lies between the ideal trigonal bipyramidal or square pyramidal environments, as suggested by the  $\tau$  value of 0.49 [58], or the SHAPE symmetry factors (Table S1) [59]. Finally, one Zn atom is coordinated in a distorted tetrahedral geometry by three O atoms from three  $\mu_{1,3}$ -bridging acetate groups and the triply bridging OH group. A selection of bond lengths and angles is given in Table 1. The bond lengths and angles show no unusual features and compare well with those in other six-, five- and four-coordinated Zn complexes. The corresponding bond lengths and angles within the two trinuclear subunits do not differ much. The angles around Zn1, for example, range from  $80.33(16)^\circ$  to  $98.8(2)^\circ$  and from  $78.95(16)^\circ$  to  $98.98(19)^\circ$  for the corresponding Zn4 atom in the other  $[\text{Zn}_3\text{L}(\text{OH})(\text{OAc})_2]^{2+}$  fragment. The structure of **1** is very similar to that of the hexanuclear complex  $[\text{Zn}_6\text{L}'_2(\text{OH})_2(\text{OAc})_8]$  supported by the ligand 2,6-bis((N-benzyl)iminomethyl)-4-methylphenol. This complex is also composed of trinuclear  $[\text{Zn}_3\text{L}(\text{OH})(\text{OAc})_2]^{2+}$  moieties [11]. Other polynuclear zinc carboxylato complexes are known; basic zinc acetate,  $\text{Zn}_4\text{O}(\text{CH}_3\text{COO})_6$ , is a prominent example [60].

**Table 1.** Selected bond lengths (Å) and angles (°) for 1·3MeCN·0.5H<sub>2</sub>O.

Zn1-O1 2.114(4)	N1-Zn1-O1 87.90(19)	N3-Zn4-O11 88.40(18)
Zn1-N1 2.064(5)	N1-Zn1-O3 97.27(17)	N3-Zn4-O13 90.8(2)
Zn1-O2 2.016(4)	N1-Zn1-O4 86.15(16)	N3-Zn4-O14 88.41(19)
Zn1-O3 2.103(4)	N1-Zn1-O5 98.8(2)	N3-Zn4-O15 98.98(19)
Zn1-O4 2.264(4)	O1-Zn1-O4 94.19(16)	O11-Zn4-O14 93.16(16)
Zn1-O5 2.101(4)	O2-Zn1-N1 163.88(19)	O12-Zn4-N3 166.20(19)
Zn2-O1 2.063(4)	O2-Zn1-O1 78.83(16)	O12-Zn4-O11 78.95(16)
Zn2-N2 2.091(5)	O2-Zn1-O3 92.02(16)	O12-Zn4-O13 94.78(18)
Zn2-O2 2.065(4)	O2-Zn1-O4 85.74(15)	O12-Zn4-O14 86.82(17)
Zn2-O6 2.060(4)	O2-Zn1-O5 93.55(17)	O12-Zn4-O15 93.07(17)
Zn2-O7 1.996(4)	O3-Zn1-O1 90.56(17)	O13-Zn4-O11 90.37(18)
Zn3-O2 1.939(4)	O3-Zn1-O4 174.26(17)	O13-Zn4-O14 176.35(18)
Zn3-O8 1.976(4)	O5-Zn1-O1 170.98(16)	O15-Zn4-O11 170.48(16)
Zn3-O9 1.957(4)	O5-Zn1-O3 94.56(17)	O15-Zn4-O13 95.50(18)
Zn3-O10 1.969(4)	O5-Zn1-O4 80.33	O15-Zn4-O14 81.13(16)
Zn4-O11 2.113(4)	O1-Zn2-N2 88.07(19)	N4-Zn5-O11 87.19(19)
Zn4-N3 2.034(5)	O1-Zn2-O2 78.89(16)	O12-Zn5-N4 164.02(19)
Zn4-O12 2.012(4)	O2-Zn2-N2 156.16(18)	O12-Zn5-O11 79.39(16)
Zn4-O13 2.107(4)	O6-Zn2-N2 89.1(2)	O12-Zn5-O16 95.29(19)
Zn4-O14 2.234(4)	O6-Zn2-O1 148.89(19)	O16-Zn5-N4 88.1(2)
Zn4-O15 2.096(4)	O6-Zn2-O2 91.90(18)	O16-Zn5-O11 135.03(19)
Zn5-O12 2.045(4)	O7-Zn2-N2 105.0(2)	O17-Zn5-N4 96.70(19)
Zn5-N4 2.059(5)	O7-Zn2-O1 109.06(18)	O17-Zn5-O11 115.40(19)
Zn5-O11 2.063(4)	O7-Zn2-O2 98.14(17)	O17-Zn5-O12 96.87(19)
Zn5-O16 2.046(5)	O7-Zn2-O6 101.6(2)	O17-Zn5-O16 109.6(2)
Zn5-O17 2.000(4)	O2-Zn3-O8 107.92(19)	O12-Zn6-O18 106.5(2)
Zn6-O12 1.934(4)	O2-Zn3-O9 108.63(17)	O12-Zn6-O19 108.21(18)
Zn6-O18 1.952(5)	O2-Zn3-O10 122.87(18)	O12-Zn6-O20 121.79(19)
Zn6-O19 1.966(4)	O9-Zn3-O8 108.25(19)	O18-Zn6-O19 106.9(2)
Zn6-O20 1.940(4)	O9-Zn3-O10 107.01(18)	O20-Zn6-O18 107.7(2)
	O10-Zn3-O8 101.30(19)	O20-Zn6-O19 104.93(19)

Single crystals of [Zn<sub>4</sub>L<sub>4</sub>(μ-OH)<sub>2</sub>](ClO<sub>4</sub>)<sub>2</sub>·3MeOH·0.5MeCN (2·3MeOH·0.5MeCN) suitable for X-ray crystallographic analyses were grown by the slow evaporation of a mixed DCM/MeOH/MeCN (3:2:1) solution. The perchlorate salt crystallizes in the monoclinic space group *P*2<sub>1</sub>/*n* with four formula units per unit cell. Figure 3 displays the structure of the tetranuclear Zn complex. Selected bond lengths and angles are listed in Table 2. The crystal structure is composed of tetranuclear [Zn<sub>4</sub>L<sub>4</sub>(μ-OH)<sub>2</sub>]<sup>2+</sup> complexes, perchlorate ions and co-crystallized MeOH and MeCN molecules. The two [Zn<sub>2</sub>L<sub>2</sub>]<sup>2+</sup> fragments are joined via two bridging hydroxido ligands to generate the [Zn<sub>4</sub>L<sub>4</sub>(μ-OH)<sub>2</sub>]<sup>2+</sup> complex's dication. The Zn<sup>2+</sup> ions are all five-coordinated, and they are surrounded by two imine N and two bridging phenolate O atoms from the supporting ligand and one bridging hydroxido ligand. The τ values range from 0.49 to 0.52, indicating that the coordination geometries of the Zn<sup>2+</sup> ions lie in between the ideal trigonal bipyramidal or square pyramidal environments. This is also supported by the SHAPE symmetry factors given in Table S1. The Zn-N bond distances between 2.048(3) and 2.118(3) Å as well as the Zn-O distances between 1.962(2) and 2.154(2) Å are all within the usual ranges for such complexes.



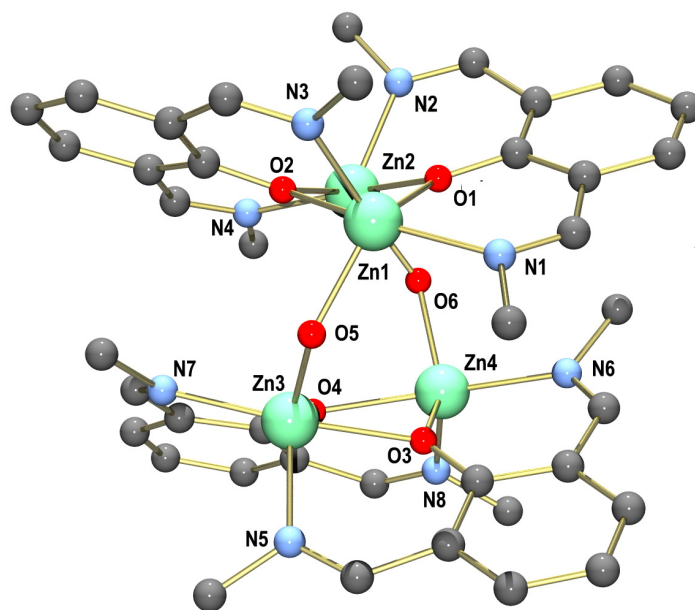


**Figure 3.** Molecular structure of the  $[Zn_4L_4(\mu-OH)_2]^{2+}$  complex cation in the crystals of (2:3MeOH-0.5MeCN). All hydrogen atoms, phenyl rings and *t*-Bu groups have been omitted for clarity.

**Table 2.** Selected bond lengths (Å) and angles (°) for 2:3MeOH-0.5MeCN.

Zn1-O1 2.018(3)	N1-Zn1-O2 159.01(11)	N5-Zn3-N7 118.88(11)
Zn1-O2 2.135(2)	N3-Zn1-N1 107.88(12)	N5-Zn3-O3 84.91(10)
Zn1-N1 2.117(3)	N3-Zn1-O2 85.17(12)	N7-Zn3-O3 157.33(11)
Zn1-N3 2.048(3)	O1-Zn1-N1 86.28(11)	O4-Zn3-N5 115.58(11)
Zn1-O5 1.956(2)	O1-Zn1-N3 119.00(12)	O4-Zn3-N7 86.56(11)
Zn2-O1 2.144(2)	O5-Zn1-N1 99.91(11)	O4-Zn3-O3 72.08(9)
Zn2-O2 2.012(3)	O5-Zn1-N1 99.91(11)	O5-Zn3-N5 108.29(12)
Zn2-N2 2.050(3)	O5-Zn1-N3 119.00(12)	O5-Zn3-N7 99.47(11)
Zn2-N4 2.118(3)	O5-Zn1-O1 129.36(10)	O5-Zn3-O3 88.85(10)
Zn2-O6 1.992(3)	O5-Zn1-O2 91.57(10)	O5-Zn3-O4 129.58(10)
Zn3-O3 2.154(2)	N2-Zn2-N4 110.11(11)	N6-Zn4-O4 160.17(11)
Zn3-O4 2.008(3)	N2-Zn2-O1 85.85(10)	N8-Zn4-N6 108.65(11)
Zn3-N5 2.053(3)	N4-Zn2-O1 158.57(11)	N8-Zn4-O4 84.43(11)
Zn3-N7 2.118(3)	O2-Zn2-N2 115.58(12)	O3-Zn4-N6 88.07(11)
Zn3-O5 1.962(2)	O2-Zn2-N4 87.08(12)	O3-Zn4-N8 116.03(11)
Zn4-O3 2.003(2)	O2-Zn2-O1 72.81(9)	O3-Zn4-O4 72.58(9)
Zn4-O4 2.135(2)	O6-Zn2-N2 110.14(12)	O6-Zn4-N6 98.18(11)
Zn4-N6 2.076(3)	O6-Zn2-N4 98.46(11)	O6-Zn4-N8 109.84(11)
Zn4-N8 2.055(3)	O6-Zn2-O1 88.76(10)	O6-Zn4-O3 128.75(10)
Zn4-O5 1.993(2)	O6-Zn2-O2 128.62(11)	O6-Zn4-O3 90.88(10)

### 3.3. Electronic Absorption and Emission Spectroscopy

The synthesized compounds were further characterized using UV-vis absorption and photoluminescence spectroscopy. The electronic absorption spectra for the free ligand **HL** and its deprotonated phenolate form, **L<sup>-</sup>**, were measured in a mixture of DCM/MeCN (3:2) at room temperature. The spectrum of the free ligand displays three main absorption



maxima (Figure 4). The absorption maxima and corresponding extinction coefficients are listed in Table 3.

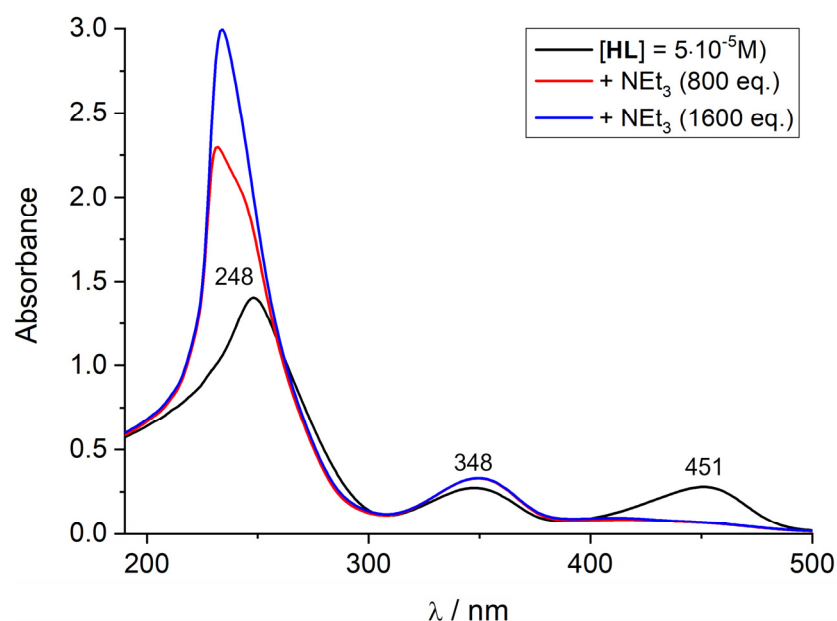


**Figure 4.** Measured UV-vis spectra of **HL** and its deprotonated form, **L<sup>-</sup>**. Experimental conditions:  $5 \times 10^{-5}$  M,  $\text{CH}_2\text{Cl}_2/\text{MeOH}$  ( $v:v/3:2$ ), 298 K. The fully deprotonated ligand was obtained by adding an excess of  $\text{NEt}_3$  to the solution of **HL**.

The broad band with an absorption maximum at 248 nm is attributed to the  $\pi$ - $\pi^*$  transitions localized on the phenol and phenyl rings of **HL**, according to time-dependent density functional theory (TDDFT) calculations (see details below). The lower-energy bands with absorption maxima at 348 nm and 451 nm, on the other hand, are assigned to electronic transitions within a more extended  $\pi$  system involving the phenolate ring and the two imine groups. The UV-vis spectrum of the deprotonated ligand differs significantly from that of the protonated ligand. It reveals two well-resolved absorption maxima at 234 and 349 nm. Instead of the band at 450 nm observed in **HL**, there is a tail on the 349 nm band that extends into the visible range but with no well-developed maximum. Thus, deprotonation has a strong effect on the spectroscopic properties of **HL**.

**Table 3.** UV-vis spectroscopic data for **HL** and the deprotonated ligand; luminescence spectroscopic data for **HL**, **L<sup>-</sup>** and **1**.

	$\lambda_{\text{max}}/\text{nm}$	$\epsilon\lambda/[\text{M}^{-1}\text{cm}^{-1}]$	Assignment
<b>HL(a)</b>	451	5600	$\pi$ - $\pi^*$ (ArOH)
	348	5480	$\pi$ - $\pi^*$ (ArOH)
	248	28,800	$\pi$ - $\pi^*$ (ArOH+Ph)
<b>L<sup>-</sup>(a,b)</b>	349	6620	$\pi$ - $\pi^*$ (ArO <sup>-</sup> )
	232	45,940	$\pi$ - $\pi^*$ (ArO <sup>-</sup> )
<b>L<sup>-</sup>(a,c)</b>	349	6640	$\pi$ - $\pi^*$ (ArO <sup>-</sup> )
	234	59,920	$\pi$ - $\pi^*$ (ArO <sup>-</sup> )
	$\lambda_{\text{ex}}/\text{nm}$	$\lambda_{\text{em}}/\text{nm}$	Stokes shift/ $\text{cm}^{-1}$ (rel. intensity/a.u.)
<b>HL(d)</b>	447	497	2250 (5380)
<b>L<sup>-</sup>(b,d)</b>	346	563	11,139 (350)
<b>1(d)</b>	378	452	4331 (35,850)

(a) DCM/MeOH (3:2/ $v:v$ ),  $10^{-5}$  M sample concentration, (b)  $[\text{NEt}_3] = 8 \times 10^{-3}$  M, (c)  $[\text{NEt}_3] = 16 \times 10^{-3}$  M, (d) MeCN,  $10^{-5}$  M sample concentration.

To study the complexation reactions of **HL** with  $\text{Zn}^{2+}$  ions in the solution, UV-vis spectrophotometric batch titrations were carried out. The method of YOE and JONES was used here, in which the ligand concentration is kept constant over the entire range and the amount of  $\text{Zn}^{2+}$  is raised stepwise until a stable complex species is formed [61–64]. Tetra-*n*-butylammonium hexafluorophosphate (10 mM) was added to the used solvent mixture (3:2—DCM/MeOH) to ensure a constant ionic strength during the complexation reactions.

The addition of aliquots of  $\text{Zn}(\text{OAc})_2$  (from 0.1 to 10 equiv.) leads to clear changes in the UV-vis spectrum of the ligand (Figure 5). Thus, the bands at 350 and 450 nm for **HL** vanish with increasing  $\text{Zn}^{2+}$  concentrations, and a new band with a maximum at 387 nm emerges (at a Zn/L ratio of 1.0 equiv.), providing clear support that  $\text{Zn}^{2+}$  binding to the bis(iminophenolate)ligand **L**<sup>−</sup> occurs. Adding the further equivalents of  $\text{Zn}(\text{OAc})_2$  leads to a weak but significant hyperchromic effect manifested by the slight increase in the intensity of the 387 nm band. The YOE and JONES method was applied in order to determine the stoichiometric ratio of the complex. As observed from the inset of Figure 5, the plot of the absorbance value versus stoichiometric ratio  $[\text{Zn}^{2+}]/[\text{HL}]$  increases very steeply up to 1:1, and then there is a further, but much less pronounced, increase in intensity, suggesting that additional  $\text{Zn}^{2+}$  ions will not directly interact with the donor atoms of **HL**. The spectroscopic titration of **HL** with  $\text{Zn}(\text{ClO}_4)_2 \cdot 6\text{H}_2\text{O}$  behaved in a very similar fashion (SI). Overall, these findings suggest that the ligand examined here has a strong propensity to form  $\text{Zn}^{2+}$  complexes with a 1:1 metal/ligand ratio. This ratio would be consistent with the 2:2 stoichiometries found in the solid state and implies that such 2:2 complexes also exist in the solution state. In the presence of additional co-ligands, this ratio may be increased, but it is accompanied by much less pronounced changes in the spectroscopic features of supporting ligand **HL**. These findings are also consistent with those made by fluorescence spectroscopy described below.

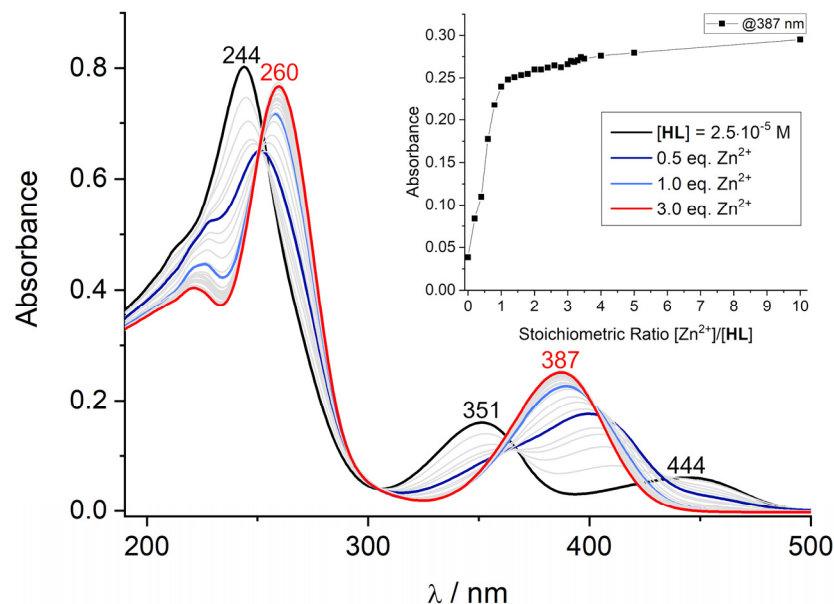


**Figure 5.** Spectrophotometric titration of **HL** with  $\text{Zn}(\text{OAc})_2 \cdot 2\text{H}_2\text{O}$  in  $\text{CH}_2\text{Cl}_2/\text{MeOH}$  (3:2/*v:v*) at a  $10^{-5}$  M concentration and constant ionic strength ( $10^{-2}$  M  $\text{N}(\text{n-Bu})_4\text{PF}_6$ ,  $T = 295$  K). The red curve corresponds to the final  $\text{Zn}^{2+}/\text{HL}$  stoichiometric ratio of 3.0. The inset shows the evolution of selected absorbance values versus the  $[\text{Zn}^{2+}]/[\text{HL}]$  stoichiometric ratio.

The complexation reactions were further examined using fluorescence spectroscopy. The emission spectra of compounds **HL**, **L**<sup>−</sup>, and of a 1:3 solution of **HL** and  $\text{Zn}(\text{OAc})_2$  are displayed in Figure 6 along with the corresponding excitation spectra. The emission spectra were measured in acetonitrile solution at the  $10^{-5}$  M concentration. Table 3 lists the data. The free ligand fluorescence is blue-green, reflected in a single emission band with

a maximum at 497 nm when excited at 447 nm. The excitation spectrum of **HL** monitored at 497 nm corresponds to the absorption spectrum and reveals an absorption band at 447 nm that is assigned to a transition into the  $^1(\pi-\pi^*)$  state of the bis(iminomethyl)phenol system. The deprotonation of the ligand has a strong effect on the luminescence properties. This can be detected by the naked eye. Thus, in contrast to **HL**, **L<sup>-</sup>** exhibits a very weak, intraligand  $^1(\pi-\pi^*)$  fluorescence emission band at 563 nm. The luminescence intensity decreases by a factor of 15, and the Stokes shift increases from 2250  $\text{cm}^{-1}$  for **HL** to 11,139  $\text{cm}^{-1}$  in **L<sup>-</sup>**. Remarkably, the complexation of the ligand by  $\text{Zn}^{2+}$  leads to a circa six-fold enhancement of the luminescence intensity, which is also accompanied by a hypsochromic shift in the emission band to 452 nm. This behavior has been observed for other  $\text{Zn}^{2+}$  complexes supported by *o*-hydroxy-aryl SCHIFF base ligands [65–68]. The enhancement of the emission intensity can be explained by the CHEF effect (*chelation-enhanced fluorescence effect*) due to the inhibition of photo-induced electron transfer processes [69,70].

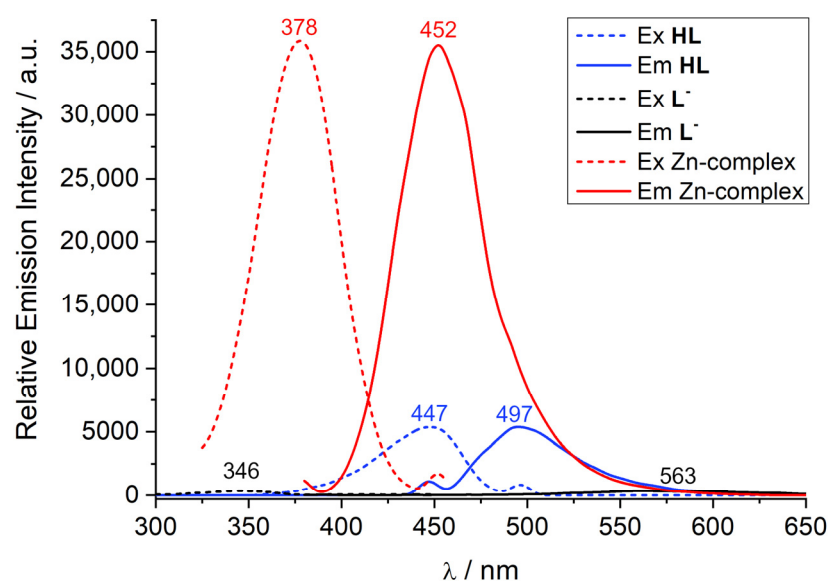


**Figure 6.** Excitation (dashed) and emission spectra (solid) of **HL**, **L<sup>-</sup>**, and a 1:3 mixture of **HL**/ $\text{Zn}(\text{OAc})_2$  in MeCN ( $10^{-5}$  M, 298 K).

Figure 7 displays a titration of **HL** with  $\text{Zn}(\text{OAc})_2$  monitored by fluorescence spectroscopy at 0.01 mM concentration. As observed, the intensity of the emission band at around 450 nm increases steadily with increasing  $\text{Zn}^{2+}$  concentrations. An inflection point occurs at a metal-to-ligand ratio (M/L) of 1:1. At higher M/L ratios, the emission intensity remains nearly constant. These observations are in good agreement with the conclusions provided by UV vis spectroscopy and provide strong support for the presence of  $\text{Zn}^{2+}$  complexes with 1:1 M/L ratio. The slight blue shift of the maximum of the emission band from 450 to 445 nm may be due to the change in the coordination geometry of the initial coordination geometry, such as an attachment of additional acetate or hydroxide ligands, although other factors cannot be ruled out.

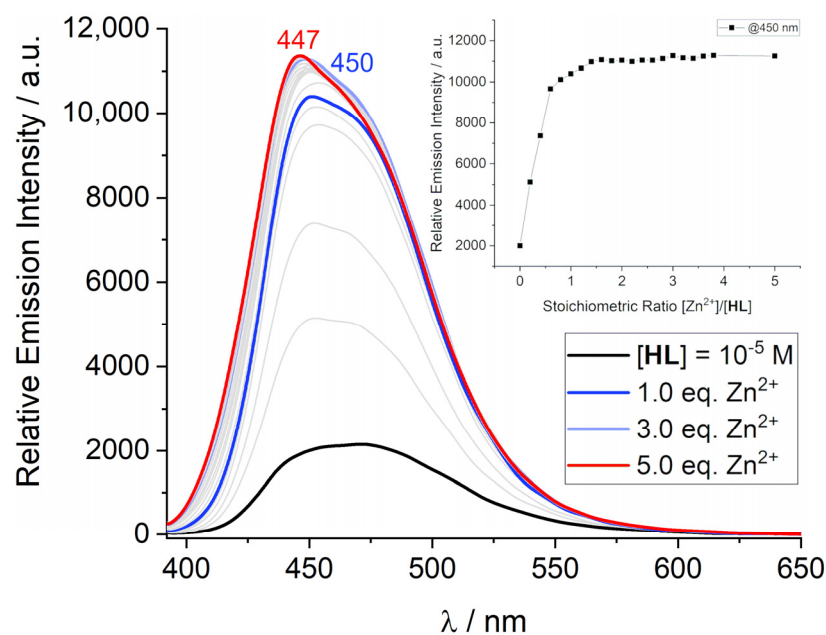


**Figure 7.** Fluorescence titration of **HL** with  $\text{Zn}(\text{OAc})_2 \cdot 2\text{H}_2\text{O}$  in  $\text{CH}_2\text{Cl}_2/\text{MeOH}$  (3:2/*v:v*) at a  $10^{-5}$  M concentration and constant ionic strength ( $10^{-2}$  M  $\text{N}(\text{n-Bu})_4\text{PF}_6$ ,  $T = 295$  K,  $\lambda_{\text{exc}} = 378$  nm). The blue and red curves correspond to  $\text{Zn}^{2+}/\text{HL}$  stoichiometric ratios of 1.0 and 5.0, respectively. The inset shows the evolution of the fluorescence intensity of the emission band at 450 nm versus the  $[\text{Zn}^{2+}]/[\text{HL}]$  stoichiometric ratio.

The luminescence properties of the ligand **HL** were investigated in the presence of other metal ions in view of reports from the literature that *o*-hydroxy-aryl compounds allow for the sensitive optical detection of  $\text{Zn}^{2+}$  ions among other metal cations [11]. Thus, methanolic solutions containing the equimolar quantities of the ligand and a series of abundant and biologically relevant *p*- and *d*-block metals were prepared, and their emission properties were determined. Figure 8 shows that none of the investigated metal ions reveals a fluorescence enhancement. This is either attributed to the poor binding affinity of some metal ions to the SCHIFF-base ligands (in the case of  $\text{Na}^+$ ,  $\text{K}^+$ ,  $\text{Mg}^{2+}$  and  $\text{Ca}^{2+}$ ) or the quenching of the excited singlet states by electron transfer reactions involving the *d*-states of open-shell transition metal ions (in case of  $\text{Mn}^{2+}$ ,  $\text{Fe}^{2+}$ ,  $\text{Co}^{2+}$ ,  $\text{Ni}^{2+}$  and  $\text{Cu}^{2+}$ ).

Several other fluorescent OFF-ON sensors for  $\text{Zn}^{2+}$  ions based on salicylidene aldimine binding sites have been reported [11,20,65].  $\text{Zn}^{2+}$  binding enhances the rather weak intraligand  $^1(\pi-\pi)$  fluorescence emission of the free ligands significantly due to the inhibition of photo-induced electron transfer processes [65].  $\text{Zn}^{2+}$  ion binding also rigidifies the ligand architecture, thereby decreasing the probability of the vibrational deactivation of the excited singlet state [34,35].

The fluorescence intensity of **HL** as a function of the  $\text{Zn}^{2+}$  concentration was investigated in order to determine the LOD value (limit of detection value), which provides the lowest concentration that can be measured. Fluorescence intensity was found to be linear between  $1 \times 10^{-6}$  and  $1 \times 10^{-7}$  M  $\text{Zn}^{2+}$  and produced an LOD value of 0.24(1) ppm. This value is comparable to those of other  $\text{Zn}^{2+}$  fluorescence sensor systems featuring iminophenolate units [11,34,35].

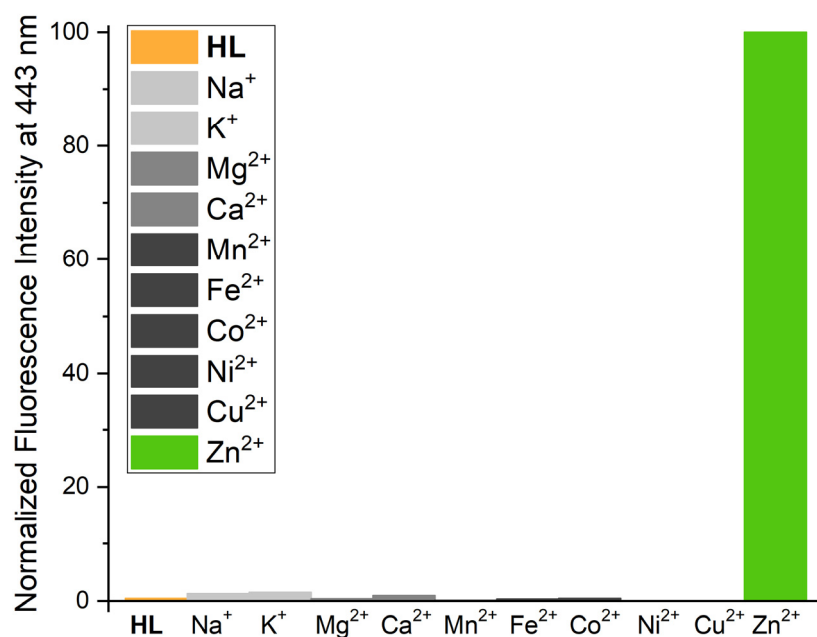


**Figure 8.** Normalized emission intensity at 443 nm of  $10^{-5}$  M solutions containing equimolar quantities of **HL** and various metal ions (methanolic solution, concentration: ligand  $1 \times 10^{-5}$  M, metal salt:  $3 \times 10^{-5}$  M,  $T = 295$  K); excitation wavelength 378 nm.

In order to support experimental findings, we have carried out TD-DFT calculations on ligand **HL**, differently (de-)protonated species and a  $[\text{Zn}_2\text{L}_2]^{2+}$  complex to simulate the UV-vis absorption spectra (for details, see the Experimental Section). By considering various forms of **HL**, dynamic and solvent effects could be accounted for, allowing the full assignment of absorption bands in the experimental spectra (see Figure 9).

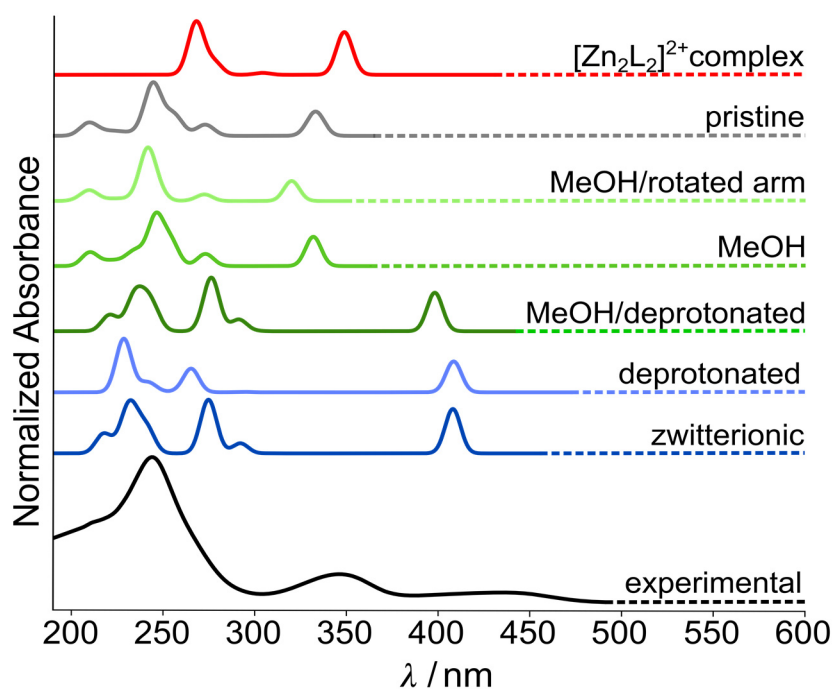


**Figure 9.** Simulated UV-vis spectra of different **HL** forms. Included are the zwitterionic form, explicitly coordinated methanol, deprotonated **HL**, the pristine ligand and the  $[\text{Zn}_2\text{L}_2]^{2+}$  complex. The spectra were obtained using AMS code [53].

The band with the largest intensity was assigned to various  $\pi$ - $\pi^*$  transitions, while the band at around 350 nm was assigned to a  $\pi$ - $\pi^*$  transition with a contribution from the  $n$ -orbitals of the OH group. The lowest excitations at 450 nm were assigned to a  $\pi$ - $\pi^*$  transition with contributions from the deprotonated phenol group, and it was observed that the deprotonation resulted in a large redshift into the visible light range. As it is shown in Figure 10 the experimental results are in good agreement with the calculated ones.

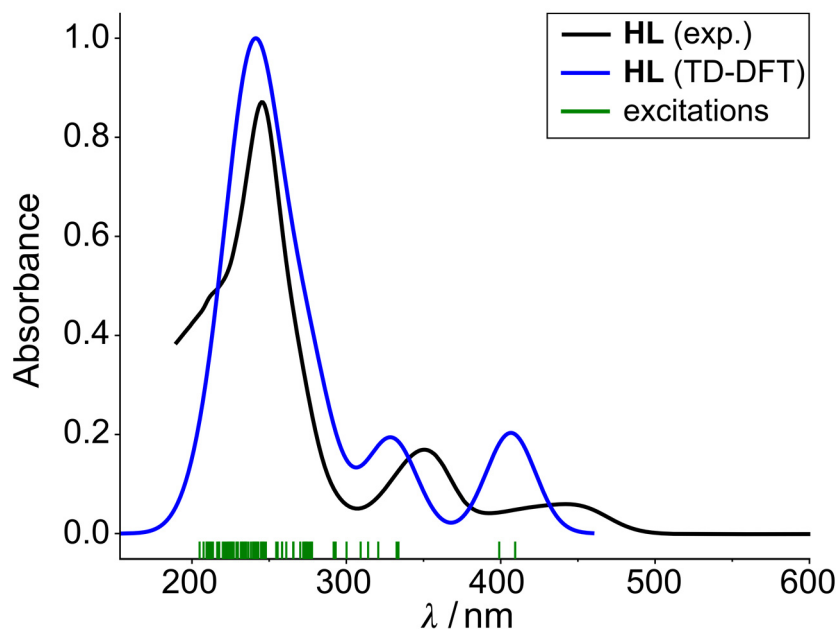


**Figure 10.** Summation of the calculated excitations for all species in Figure 9. The excitations are convolved with a 30 nm wide Gaussian to fit the experimental spectrum well.

#### 4. Conclusions

The syntheses of the new tridentate Schiff-base ligand 2,6-bis((*N*-benzyl)iminomethyl)-4-*tert*-butylphenol (**HL**) and the corresponding polynuclear zinc complexes  $[\text{Zn}_6\text{L}_2(\mu_3\text{-OH})_2(\text{OAc})_8]$  (**1**) and  $[\text{Zn}_4\text{L}_4(\mu_2\text{-OH})_2](\text{ClO}_4)_2$  (**2**) are described. The exact composition of the two complexes was confirmed via X-ray crystallography, which revealed the influence of the coordinating acetate anion. The molecular structure of **1** contains  $\text{Zn}^{2+}$  ions, which are six-, five- and four-coordinated by the O and the two N atoms of the ligand and OH<sup>−</sup> and acetate ligands. In the discrete complex cation  $[\text{Zn}_4\text{L}_4(\mu_2\text{-OH})_2]^{2+}$  of **2** all  $\text{Zn}^{2+}$  ions, there are five-coordinated with  $\tau$  values ranging from 0.49 to 0.52. The absorption properties of the ligand have been investigated with UV-vis spectroscopy. The lower energy band at 348 nm and the visible transition at 451 nm are designated as electronic transitions within the extended  $\pi$  system of the iminophenolate. Via the deprotonation of the ligand, the band at 451 nm disappears, whereby the spectroscopic properties of the ligand change significantly. The UV-vis titrations with the acetate and the perchlorate salts of  $\text{Zn}^{2+}$  exhibit the tendency of **HL** to form complexes with a stoichiometric ratio of 1:1. The results of luminescence spectroscopy studies support this observation. The complexation of  $\text{Zn}^{2+}$  leads to a further enhancement of the fluorescence intensity by factor six (CHEF effect), which was not detected for  $\text{Na}^+$ ,  $\text{K}^+$ ,  $\text{Mg}^{2+}$ ,  $\text{Ca}^{2+}$ ,  $\text{Mn}^{2+}$ ,  $\text{Fe}^{2+}$ ,  $\text{Co}^{2+}$ ,  $\text{Ni}^{2+}$  or  $\text{Cu}^{2+}$ .

**Supplementary Materials:** The following supporting information can be downloaded at: <https://www.mdpi.com/article/10.3390/chemistry5020070/s1>. Figure S1: FTIR spectrum of HL (KBr pellet); Figure S2: FTIR spectra of  $[\text{Zn}_6\text{L}_2(\text{OH})_2(\text{OAc})_8]$  (**1**, KBr pellet) and  $[\text{Zn}_4\text{L}_4(\text{OH})_2](\text{ClO}_4)_2$  (**2**, KBr pellet); Figure S3: Overlay of the FTIR spectra of the ligand (HL) and the zinc complexes **1** and **2** (1700–1500  $\text{cm}^{-1}$ ); Figure S4: Overlay of the FTIR spectra of the zinc complexes **1** and **2** (1750–450  $\text{cm}^{-1}$ ); Figure S5: Packing diagram of HL showing intermolecular  $\pi$ - $\pi$  stacking (offset face-to-face) interactions between adjacent ligand molecules; Figure S6:  $^{13}\text{C}$ -NMR spectrum of HL recorded in dimethylsulfoxide- $d_6$  at 363 K; multiplicity of C-H coupling displayed; parts of the spectrum



without signals cut out for better observation of the multiplicities; Figure S7:  $^1\text{H}$ -NMR spectrum of  $[\text{Zn}_6\text{L}_2(\text{OH})_2(\text{OAc})_8]$  recorded in  $\text{CD}_3\text{CN}$  at ambient temperature; Figure S8: Spectrophotometric titration of HL with  $\text{Zn}(\text{ClO}_4)_2 \cdot 6 \text{H}_2\text{O}$  in  $\text{CH}_2\text{Cl}_2/\text{MeOH}$  (3:2/v:v) at a  $10^{-5}$  M concentration and constant ionic strength ( $10^{-2}$  M  $\text{N}(\text{n-Bu})_4\text{PF}_6$ ,  $T = 295$  K). The blue curve corresponds to a final  $\text{Zn}^{2+}/\text{HL}$  molar ratio of 1:1. The inset shows the evolution of selected absorbance values versus the  $[\text{Zn}^{2+}]/[\text{HL}]$  molar ratio; Figure S9: Excitation (blue) and emission spectrum (green) of HL in acetonitrile ( $c(\text{HL}) = 1 \times 10^{-5}$  M, 298 K). MeCN;  $1 \times 10^{-5}$  M;  $\lambda_{\text{Ex}} = 447$  nm;  $\lambda_{\text{Em}} = 497$  nm; Figure S10: Excitation (violet) and emission spectrum (yellow) of L- in acetonitrile in the presence of base ( $c(\text{HL}) = 1 \times 10^{-5}$  M,  $c(\text{NEt}_3) = 1 \times 10^{-5}$  M, 298 K). MeCN;  $c(\text{HL}) = 1 \times 10^{-5}$  M;  $c(\text{NEt}_3) = 1 \times 10^{-5}$  M;  $\lambda_{\text{Ex}} = 346$  nm;  $\lambda_{\text{Em}} = 563$  nm; Figure S11: Excitation (azure) and emission spectrum (turquoise) of  $[\text{Zn}_6\text{L}_2(\text{OH})_2(\text{OAc})_8]$  in acetonitrile ( $c(\text{complex}) = 1 \times 10^{-5}$  M, 298 K).  $\lambda_{\text{Ex}} = 378$  nm;  $\lambda_{\text{Em}} = 452$  nm; Figure S12: Major contributions to the observed UV-Vis bands of HL with the single orbital transition contribution in parentheses. (a) HOMO $\rightarrow$ LUMO: 334 nm (97%). (b) HOMO-1 $\rightarrow$ LUMO+1: 245 nm (67%); Figure S13: Major contributions to the observed UV-Vis bands of HL- with the single orbital transition contribution in parentheses. (a) HOMO $\rightarrow$ LUMO: 409 nm (98%). (b) HOMO-2 $\rightarrow$ LUMO+1: 229 nm (36%); Figure S14: Major contributions to the observed UV-Vis bands of  $[\text{Zn}_2\text{L}_2]^{2+}$  with the single orbital transition contribution in parentheses. (a) HOMO $\rightarrow$ LUMO: 348 nm (57%); Figure S15: PBE-D3(BJ) optimized structure of HL used for the simulation of UV-Vis spectra (pristine) and basis for the other used structures; Figure S16: Fluorescence spectra HL as a function of  $\text{Zn}^{2+}$  ion concentration; Table S1: Shape symmetry factors for complex 1.

**Author Contributions:** Conceptualization, T.S. and V.K.; methodology, T.S.; validation, T.S., B.K. and A.K.; formal analysis, H.W. and A.K.; investigation, V.K. and T.S.; resources, B.K.; data curation, B.K.; writing—original draft preparation, T.S.; writing—review and editing, M.B. and B.K.; visualization, T.S., M.B. and B.K.; supervision, B.K.; project administration, B.K.; funding acquisition, B.K. All authors have read and agreed to the published version of the manuscript.

**Funding:** This research was funded by the German Science Foundation (Priority programme 2102, “Light Controlled Reactivity of Metal Complexes”, project KE 585/9-1).

**Data Availability Statement:** Deposition Numbers 2248758–2248760 contain the supplementary crystallographic data for this paper. These data are provided free of charge by the joint Cambridge Crystallographic Data Centre and Fachinformationszentrum Karlsruhe Access Structures service. TD-DFT data will be available soon and will be announced.

**Acknowledgments:** We are thankful to H. Krautscheid for providing facilities for X-ray crystallographic measurements.

**Conflicts of Interest:** The authors declare no conflicts of interest.

## References

1. Follmer, C.; Real-Guerra, R.; Wasserman, G.E.; Olivera-Severo, D.; Carlini, C.R. Jackbean, soybean and *Bacillus pasteurii* ureases. *Eur. J. Biochem.* **2004**, *271*, 1357–1363, <https://doi.org/10.1111/j.1432-1033.2004.04046.x>.
2. Sumner, J.B. The Isolation and Crystallization of the Enzyme Urease. *J. Biol. Chem.* **1926**, *69*, 435–441, [https://doi.org/10.1016/s0021-9258\(18\)84560-4](https://doi.org/10.1016/s0021-9258(18)84560-4).
3. Bertagnolli, H.; Kaim, W. The Dinuclear CuA Center in Cytochrome c Oxidase and N2O Reductase—A Metal–Metal Bond in Biology? *Angew. Chem. Int. Ed. Engl.* **1995**, *34*, 771–773.
4. Lv, Y.; Cao, M.; Li, J.; Wang, J. A Sensitive Ratiometric Fluorescent Sensor for Zinc(II) with High Selectivity. *Sensors* **2013**, *13*, 3131–3141, <https://doi.org/10.3390/s130303131>.
5. Fernley, R.T. Non-cytoplasmic carbonic anhydrases. *Trends Biochem. Sci.* **1988**, *13*, 356–359, [https://doi.org/10.1016/0968-0004\(88\)90107-7](https://doi.org/10.1016/0968-0004(88)90107-7).
6. Hewett-Emmett, D.; Tashian, R.E. Functional diversity, conservation, and convergence in the evolution of the alpha-, beta-, and gamma-carbonic anhydrase gene families. *Mol. Phylogenetics Evol.* **1996**, *5*, 50–77.
7. Thiel, G.; Lietz, M. Regulator neuronaler Gene: Zinkfingerprotein REST. *Biol. Unserer Zeit* **2004**, *34*, 96–101, <https://doi.org/10.1002/biuz.200410244>.
8. Tashian, R.E. The carbonic anhydrases: Widening perspectives on their evolution, expression and function. *Bioessays* **1989**, *10*, 186–192, <https://doi.org/10.1002/bies.950100603>.
9. Liu, M.-J.; Bao, S.; Gálvez-Peralta, M.; Pyle, C.J.; Rudawsky, A.C.; Pavlovicz, R.E.; Killilea, D.W.; Li, C.D.; Nebert, W.; Wewers, M.D.; et al. ZIP8 Regulates Host Defense through Zinc-Mediated Inhibition of NF- $\kappa$ B. *Cell Rep.* **2013**, *3*, 386–400.
10. Ternes, W. *Biochemie der Elemente—Anorganische Chemie Biologischer Prozesse*, Springer Spektrum; Springer: Berlin/Heidelberg, Germany, 2013.



11. Roy, P.; Dhara, K.; Manassero, M.; Ratha, J.; Banerjee, P. Selective Fluorescence Zinc Ion Sensing and Binding Behavior of 4-Methyl-2,6-bis(((phenylmethyl)imino)methyl)phenol: Biological Application. *Inorg. Chem.* **2007**, *46*, 6405–6412, <https://doi.org/10.1021/ic700420w>.
12. Yu, G.; Liu, Y.; Song, Y.; Wu, X.; Zhu, D. A new blue light-emitting material. *Synth. Met.* **2001**, *117*, 211–214, [https://doi.org/10.1016/s0379-6779\(00\)00366-0](https://doi.org/10.1016/s0379-6779(00)00366-0).
13. Di Bella, S.; Fragala, I. Two-dimensional characteristics of the second-order nonlinear optical response in dipolar donor–acceptor coordination complexes. *New J. Chem.* **2002**, *26*, 285–290.
14. Leung, A.C.W.; Chong, J.H.; Patrick, B.O.; MacLachlan, M.J. Poly(salphenyleneethynylene)s: A New Class of Soluble, Conjugated, Metal-Containing Polymers. *Macromolecules* **2003**, *36*, 5051–5054.
15. Wang, P.; Hong, Z.; Xie, Z.; Tong, S.; Wong, O.; Lee, C.-S.; Wong, N.; Hung, L.; Lee, S. A bis-salicylaldiminato Schiff base and its zinc complex as new highly fluorescent red dopants for high performance organic electroluminescence devices. *Chem. Commun.* **2003**, *14*, 1664–1665, <https://doi.org/10.1039/b303591c>.
16. Rigamonti, L.; Demartin, F.; Forni, A.; Righetto, S.; Pasini, A. Copper(II) Complexes of salen Analogues with Two Differently Substituted (Push–Pull) Salicylaldehyde Moieties. A Study on the Modulation of Electronic Asymmetry and Nonlinear Optical Properties. *Inorg. Chem.* **2006**, *45*, 10976–10989.
17. Zhang, G.; Yang, G.; Wang, S.; Chen, Q.; Ma, J.S. A Highly Fluorescent Anthracene-Containing Hybrid Material Exhibiting Tunable Blue–Green Emission Based on the Formation of an Unusual “T-Shaped”. *Excimer Chem. Eur. J.* **2007**, *13*, 3630–3635.
18. Kotova, O.; Semenov, S.; Eliseeva, S.; Troyanov, S.; Lyssenko, K.; Kuzmina, N. New Helical Zinc Complexes with Schiff Base Derivatives of  $\beta$ -Diketones or  $\beta$ -Keto Esters and Ethylenediamine. *Eur. J. Inorg. Chem.* **2009**, *2009*, 3467–3474.
19. Hai, Y.; Chen, J.-J.; Zhao, P.; Lv, H.; Yu, Y.; Xu, P.; Zhang, J.-L. Luminescent zinc salen complexes as single and two-photon fluorescence subcellular imaging probes. *Chem. Commun.* **2011**, *47*, 2435–2437.
20. Dumur, F.; Contal, E.; Wantz, G.; Gigmes, D. Photoluminescence of Zinc Complexes: Easily Tunable Optical Properties by Variation of the Bridge Between the Imido Groups of Schiff Base Ligands. *Eur. J. Inorg. Chem.* **2014**, *2014*, 4186–4198, <https://doi.org/10.1002/ejic.201402422>.
21. Su, Q.; Wu, Q.-L.; Li, G.-H.; Liu, X.-M.; Mu, Y. Bis-salicylaldiminato zinc complexes: Syntheses, characterization and luminescent properties. *Polyhedron* **2007**, *26*, 5053–5060, <https://doi.org/10.1016/j.poly.2007.07.006>.
22. Cheng, J.; Ma, X.; Zhang, Y.; Liu, J.; Zhou, X.; Xiang, H. Optical Chemosensors Based on Transmetalation of Salen-Based Schiff Base Complexes. *Inorg. Chem.* **2014**, *53*, 3210–3219, <https://doi.org/10.1021/ic5000815>.
23. Malthus, S.J.; Cameron, S.A.; Brooker, S. Improved Access to 1,8-Diformyl-carbazoles Leads to Metal-Free Carbazole-Based [2 + 2] Schiff Base Macrocycles with Strong Turn-On Fluorescence Sensing of Zinc(II) Ions. *Inorg. Chem.* **2018**, *57*, 2480–2488, <https://doi.org/10.1021/acs.inorgchem.7b02763>.
24. Zhou, X.; Yu, B.; Guo, Y.; Tang, X.; Zhang, H.; Liu, W. Both Visual and Fluorescent Sensor for  $Zn^{2+}$  Based on Quinoline Platform. *Inorg. Chem.* **2010**, *49*, 4002–4007, <https://doi.org/10.1021/ic901354x>.
25. Frederickson, C.J.; Kasarskis, E.J.; Ringo, D.; Frederickson, R.E. A quinoline fluorescence method for visualizing and assaying the histochemically reactive zinc (bouton zinc) in the brain. *J. Neurosci. Methods* **1987**, *20*, 91–103, [https://doi.org/10.1016/0165-0270\(87\)90042-2](https://doi.org/10.1016/0165-0270(87)90042-2).
26. Nasir, M.S.; Fahrni, C.J.; Suhy, D.A.; Kolodnick, K.J.; Singer, C.P.; O’Halloran, T.V. The chemical cell biology of zinc: Structure and intracellular fluorescence of a zinc-quinolinesulfonamide complex. *JBIC J. Biol. Inorg. Chem.* **1999**, *4*, 775–783, <https://doi.org/10.1007/s007750050350>.
27. Coyle, P.; Zalewski, P.D.; Philcox, J.C.; Forbes, I.J.; Ward, A.D.; Lincoln, S.F.; Mahadevan, I.; Roife, A.M. Measurement of zinc in hepatocytes by using a fluorescent probe, zinquin: Relationship to metallothionein and intracellular zinc. *Biochem. J.* **1994**, *303*, 781–786, <https://doi.org/10.1042/bj3030781>.
28. Zalewski, P.D.; Forbes, I.J.; Betts, W.H. Correlation of apoptosis with change in intracellular labile Zn(II) using zinquin [(2-methyl-8-p-toluenesulphonamido-6-quinolyloxy)acetic acid], a new specific fluorescent probe for Zn(II). *Biochem. J.* **1993**, *296*, 403–408.
29. Mahadevan, I.B.; Kimber, M.C.; Lincoln, S.F.; Tiekink, E.R.T.; Ward, A.D.; Betts, W.H.; Forbes, I.J.; Zalewski, P.D. The Synthesis of Zinquin Ester and Zinquin Acid, Zinc(II)-Specific Fluorescing Agents for Use in the Study of Biological Zinc(II). *Aust. J. Chem.* **1996**, *49*, 561–568, <https://doi.org/10.1071/ch9960561>.
30. Toroptsev, I.V.; Eshchenko, V.A. Histochemical detection of zinc using fluorescent 8-(arenesulfonilamino)-quinolines. *Tsitologiya* **1970**, *12*, 1481–1484.
31. Ullmann, S.; Börner, M.; Kahnt, A.; Abel, B.; Kersting, B. Green-Emissive  $Zn^{2+}$  Complex Supported by a Macrocyclic Schiff-Base/Calix[4]arene-Ligand: Crystallographic and Spectroscopic Characterization. *Eur. J. Inorg. Chem.* **2021**, *36*, 3691–3698.
32. Laube, C.; Taut, J.A.; Kretschmar, J.; Zahn, S.; Knolle, W.; Ullmann, S.; Kahnt, A.; Kersting, B.; Abel, B. Light controlled oxidation by supramolecular Zn(ii) Schiff-base complexes. *Inorg. Chem. Front.* **2020**, *7*, 4333–4346, <https://doi.org/10.1039/d0qi00980f>.
33. Klose, J.; Severin, T.; Hahn, P.; Jeremies, A.; Bergmann, J.; Fuhrmann, D.; Griebel, J.; Abel, B.; Kersting, B. Coordination chemistry and photoswitching of dinuclear macrocyclic cadmium-, nickel-, and zinc complexes containing azobenzene carboxylate co-ligands. *Beilstein J. Org. Chem.* **2019**, *15*, 840–851, <https://doi.org/10.3762/bjoc.15.81>.
34. Ullmann, S.; Schnorr, R.; Laube, C.; Abel, B.; Kersting, B. Photoluminescence properties of tetrahedral zinc(ii) complexes supported by calix[4]arene-based salicylaldiminato ligands. *Dalton Trans.* **2018**, *47*, 5801–5811, <https://doi.org/10.1039/c8dt00757h>.

35. Ullmann, S.; Schnorr, R.; Handke, M.; Laube, C.; Abel, B.; Matysik, J.; Findesien, M.; Rüger, R.; Heine, T.; Kersting, B. Zn<sup>2+</sup>-Ion Sensing by Fluorescent Schiff Base Calix[4]arene Macrocycles. *Chem. Eur. J.* **2017**, *23*, 3824–3827.
36. *Spectrum FL*; PerkinElmer: Waltham, MA, USA, 2019.
37. *OriginPro 8G*; OriginLab Corporation: Northampton, MA, USA, 2009.
38. *MestReNova 14.1.0*; Mestrelab Research S.L.: Santiago de Compostela, Spain, 2019.
39. *X-AREA and X-RED 32*, V1.35; STOE & Cie GmbH: Darmstadt, Germany, 2006.
40. Sheldrick, G.M. Phase annealing in SHELX-90: Direct methods for larger structures. *Acta Crystallogr. Sect. A Found. Crystallogr.* **1990**, *46*, 467–473, <https://doi.org/10.1107/s0108767390000277>.
41. Sheldrick, G.M. Crystal structure refinement with SHELXL. *Acta Crystallogr. Sect. C Struct. Chem.* **2015**, *71*, 3–8, <https://doi.org/10.1107/s2053229614024218>.
42. Spek, A.L. *PLATON—A Multipurpose Crystallographic Tool*; Utrecht University: Utrecht, The Netherlands, 2000.
43. Dolomanov, O.V.; Bourhis, L.J.; Gildea, R.J.; Howard, J.A.K.; Puschmann, H. OLEX2: A complete structure solution, refinement and analysis program. *J. Appl. Crystallogr.* **2009**, *42*, 339–341.
44. Farrugia, L.J.; ORTEP-3 for Windows—A version of ORTEP-III with a Graphical User Interface (GUI) by J. Farrugia. *J. Appl. Cryst.* **1997**, *30*, 565.
45. Van Lenthe, E.; Baerends, E.J. Optimized Slater-type basis sets for the elements 1–118. *J. Comput. Chem.* **2003**, *24*, 1142–1156, <https://doi.org/10.1002/jcc.10255>.
46. Perdew, J.P.; Burke, K.; Ernzerhof, M. Generalized Gradient Approximation Made Simple. *Phys. Rev. Lett.* **1996**, *18*, 3865–3868.
47. Grimme, S.; Ehrlich, S.; Goerigk, L. Effect of the damping function in dispersion corrected density functional theory. *J. Comput. Chem.* **2011**, *32*, 1456–1465. doi:10.1002/jcc.21759.
48. van Gisbergen, S.; Snijders, J.; Baerends, E. Implementation of time-dependent density functional response equations. *Comput. Phys. Commun.* **1999**, *118*, 119–138, [https://doi.org/10.1016/s0010-4655\(99\)00187-3](https://doi.org/10.1016/s0010-4655(99)00187-3).
49. Seth, M.; Ziegler, T. Range-Separated Exchange Functionals with Slater-Type Functions. *J. Chem. Theory Comput.* **2012**, *8*, 901–907, <https://doi.org/10.1021/ct300006h>.
50. Marques, M.A.; Oliveira, M.J.; Burnus, T. Libxc: A library of exchange and correlation functionals for density functional theory. *Comput. Phys. Commun.* **2012**, *183*, 2272–2281, <https://doi.org/10.1016/j.cpc.2012.05.007>.
51. Lehtola, S.; Steigemann, C.; Oliveira, M.J.; Marques, M.A. Recent developments in libxc—A comprehensive library of functionals for density functional theory. *Software* **2018**, *7*, 1–5, <https://doi.org/10.1016/j.softx.2017.11.002>.
52. Rüger, R.; Franchini, M.; Trnka, T.; Yakovlev, A.; van Lenthe, E.; Philipsen, P.; van Vuren, T.; Klumpers, B.; Soin, T. AMS 2021.104 SCM, *Theoretical Chemistry*; Vrije Universiteit: Amsterdam, The Netherlands, 2021.
53. Baerends, E.J.; Ziegler, T.; Atkins, A.J.; Autschbach, J.; Bassetto, O.; Bashford, D.; Bérces, A.; Bickelhaupt, F.M.; Bo, C.; Boerrigter, P.M. et al. ADF, 2021.104, SCM, *Theoretical Chemistry*; Vrije Universiteit: Amsterdam, The Netherlands, 2021.
54. te Velde, G.; Bickelhaupt, F.M.; Baerends, E.J.; Fonseca Guerra, C.; van Gisbergen, S.J.A.; Snijders, J.G.; Ziegler, T. Chemistry with ADF. *J. Comput. Chem.* **2001**, *22*, 931–967.
55. Louwen, J.N.; Pye, C.C.; van Lenthe, E.; Austin, N.D.; McGarrity, E.S.; Xiong, R.; Sandler, S.I.; Burnett, R.I. AMS 2021.104 COSMO-RS, SCM, *Theoretical Chemistry*; Vrije Universiteit: Amsterdam, The Netherlands, 2021.
56. Pye, C.C.; Ziegler, T.; van Lenthe, E.; Louwen, J.N. An implementation of the conductor-like screening model of solvation within the Amsterdam density functional package—Part II. COSMO for real solvents. *Can. J. Chem.* **2009**, *87*, 790–797.
57. Pye, C.C.; Ziegler, T. An implementation of the conductor-like screening model of solvation within the Amsterdam density functional package. *Theor. Chem. Accounts* **1999**, *101*, 396–408, <https://doi.org/10.1007/s002140050457>.
58. Addison, A.W.; Rao, T.N.; Reedijk, J.; Van Rijn, J.; Verschoor, G.C. Synthesis, structure, and spectroscopic properties of copper(II) compounds containing nitrogen–sulphur donor ligands; the crystal and molecular structure of aq-ua[1,7-bis(N-methylbenzimidazol-2'-yl)-2,6-dithiaheptane]copper(II) perchlorate. *J. Chem. Soc. Dalton Trans.* **1984**, *7*, 1349–1356.
59. Llunell, M.; Casanova, D.; Cirera, J.; Alemany, P.; Alvarez, S. *SHAPE*; University of Barcelona: Barcelona, Spain, 2013.
60. Hirozo, K.; Yoshihiko, S. The Crystal Structure of Zinc Oxyacetate, Zn<sub>4</sub>O(CH<sub>3</sub>COO)<sub>6</sub>. *Bull. Chem. Soc. Jap.* **1954**, *27*, 112–114.
61. Yoe, J.H.; Jones, A.L. Colorimetric Determination of Iron with Disodium-1,2-dihydroxybenzene-3,5-disulfonate. *Ind. Eng. Chem. Anal. Ed.* **1944**, *16*, 111–115, <https://doi.org/10.1021/i560126a015>.
62. Yoe, J.H.; Harvey, A.E. Colorimetric Determination of Iron with 4-Hydroxybiphenyl-3-carboxylic Acid. *J. Am. Chem. Soc.* **1948**, *70*, 648–654.
63. Meyer, A.S.; Ayres, G.H. The Mole Ratio Method for Spectrophotometric Determination of Complexes in Solution. *J. Am. Chem. Soc.* **1957**, *79*, 49–53.
64. Meyer, A.S.; Ayres, G.H. The Interaction of Platinum(II) and Tin(II) Chlorides. *J. Am. Chem. Soc.* **1955**, *77*, 2671–2675.
65. Mitra, A.; Hinge, V.K.; Mittal, A.; Bhakta, S.; Guionneau, P.; Rao, C.P. A Zinc-Sensing Glucose-Based Naphthyl Imino Conjugate as a Detecting Agent for Inorganic and Organic Phosphates, Including DNA. *Chem. Eur. J.* **2011**, *17*, 8044–8047.
66. Pathak, R.K.; Dessingou, J.; Rao, C.P. Multiple Sensor Array of Mn<sup>2+</sup>, Fe<sup>2+</sup>, Co<sup>2+</sup>, Ni<sup>2+</sup>, Cu<sup>2+</sup>, and Zn<sup>2+</sup> Complexes of a Triazole Linked Imino-Phenol Based Calix[4]arene Conjugate for the Selective Recognition of Asp, Glu, Cys, and His. *Anal. Chem.* **2012**, *84*, 8294–8300.
67. Mum-midivarapu, V.V.S.; Tabbasum, K.; Chinta, J.P.; Rao, C.P. 1,3-Di-amidoquinoline conjugate of calix[4]arene (L) as a ratiometric and colorimetric sensor for Zn<sup>2+</sup>: Spectroscopy, microscopy and computational studies. *Dalton Trans.* **2012**, *41*, 1671–1674.

68. Mummidivarapu, V.V.S.; Bandaru, S.; Yarramala, D.S.; Samanta, K.D.; Mhatre, S.; Rao, C.P. Binding and Ratiometric Dual Ion Recognition of  $Zn^{2+}$  and  $Cu^{2+}$  by 1,3,5-Tris-amidoquinoline Conjugate of Calix[6]arene by Spectroscopy and Its Supramolecular Features by Microscopy. *Anal. Chem.* **2015**, *87*, 4988–4995.
69. Nugent, J.W.; Lee, H.; Lee, H.-S.; Reibenspies, J.H.; Hancock, R.D. Mechanism of chelation enhanced fluorescence in complexes of cadmium(ii), and a possible new type of anion sensor. *Chem. Commun.* **2013**, *49*, 9749–9751, <https://doi.org/10.1039/c3cc45829f>.
70. Joseph, R.; Chinta, J.P.; Rao, C.P. Lower Rim 1,3-Derivative of Calix[4]arene-Appended Salicylidene Imine (H2L): Experimental and Computational Studies of the Selective Recognition of H2L toward  $Zn^{2+}$  and Sensing Phosphate and Amino Acid by [ZnL]. *J. Org. Chem.* **2010**, *75*, 3387–3395.

**Disclaimer/Publisher's Note:** The statements, opinions and data contained in all publications are solely those of the individual author(s) and contributor(s) and not of MDPI and/or the editor(s). MDPI and/or the editor(s) disclaim responsibility for any injury to people or property resulting from any ideas, methods, instructions or products referred to in the content.